The Astrophysical Journal Supplement Series, 213:12 (14pp), 2014 July doi:10.1088/0067-0049/213/1/12

THE SLOAN DIGITAL SKY SURVEY STRIPE 82 IMAGING DATA: DEPTH-OPTIMIZED CO-ADDS OVER 300 deg^2 IN FIVE FILTERS

Linhua Jiang[1,12,13], Xiaohui Fan[2,12], Fuyan Bian[3,12,14], Ian D. McGreer[2], Michael A. Strauss[4,12], James Annis[5], Zoë Buck[4,6,12], Richard Green[2,12], Jacqueline A. Hodge[7,8,12], Adam D. Myers[9,12], Alireza Rafiee[10,12], and Gordon Richards[11,12]

[1] School of Earth and Space Exploration, Arizona State University, Tempe, AZ 85287-1504, USA
[2] Steward Observatory, University of Arizona, 933 North Cherry Avenue, Tucson, AZ 85721, USA
[3] Research School of Astronomy and Astrophysics, Australian National University, Weston Creek, ACT 2611, Australia
[4] Department of Astrophysical Sciences, Princeton University, Princeton, NJ 08544, USA
[5] Center for Particle Astrophysics, Fermi National Accelerator Laboratory, P.O. Box 500, Batavia, IL 60510, USA
[6] Department of Education, University of California, Santa Cruz 1156 High Street, Santa Cruz, CA 95064, USA
[7] NRAO, 520 Edgemont Road, Charlottesville, VA 22903, USA
[8] University of California, 1 Shields Ave, Davis, CA 95616, USA
[9] Department of Physics and Astronomy, University of Wyoming, Laramie, WY 82071, USA
[10] Department of Physics, Astronomy, and Geosciences, Towson University, Towson, MD 21252, USA
[11] Department of Physics, Drexel University, 3141 Chestnut Street, Philadelphia, PA 19104, USA
Received 2014 February 20; accepted 2014 May 28; published 2014 June 25

ABSTRACT

We present and release co-added images of the Sloan Digital Sky Survey (SDSS) Stripe 82. Stripe 82 covers an area of ∼300 deg^2 on the celestial equator, and has been repeatedly scanned 70–90 times in the *ugriz* bands by the SDSS imaging survey. By making use of all available data in the SDSS archive, our co-added images are optimized for depth. Input single-epoch frames were properly processed and weighted based on seeing, sky transparency, and background noise before co-addition. The resultant products are co-added science images and their associated weight images that record relative weights at individual pixels. The depths of the co-adds, measured as the 5σ detection limits of the aperture (3.″2 diameter) magnitudes for point sources, are roughly 23.9, 25.1, 24.6, 24.1, and 22.8 AB magnitudes in the five bands, respectively. They are 1.9–2.2 mag deeper than the best SDSS single-epoch data. The co-added images have good image quality, with an average point-spread function FWHM of ∼1″ in the *r*, *i*, and *z* bands. We also release object catalogs that were made with SExtractor. These co-added products have many potential uses for studies of galaxies, quasars, and Galactic structure. We further present and release near-IR *J*-band images that cover ∼90 deg^2 of Stripe 82. These images were obtained using the NEWFIRM camera on the NOAO 4 m Mayall telescope, and have a depth of about 20.0–20.5 Vega magnitudes (also 5σ detection limits for point sources).

Key words: atlases – catalogs – surveys

Online-only material: color figures, machine-readable table

1. INTRODUCTION

Large-area multiwavelength surveys have revolutionized our understanding of the properties of distant galaxies and quasars, as well as stars in our own Galaxy. The Sloan Digital Sky Survey (SDSS; York et al. 2000) has been a pioneer among these surveys in the last decade. The SDSS is an imaging and spectroscopic survey of the sky using a dedicated wide-field 2.5 m telescope (Gunn et al. 2006) at the Apache Point Observatory. So far the SDSS has obtained spectra of more than 1,500,000 galaxies and 160,000 quasars (Ahn et al. 2012, 2014; Pâris et al. 2012, 2014). While its imaging survey has been completed, its spectroscopic survey is still going on in the phase known as SDSS-III (Eisenstein et al. 2011), so these numbers are growing steadily.

The SDSS imaging survey covered a total of 14,555 deg^2 of unique sky area (Ahn et al. 2012). Imaging was performed in drift-scan mode using a 142 mega-pixel camera (Gunn et al. 1998) that gathers data in 5 broad bands, *ugriz*, on moonless photometric (Hogg et al. 2001) nights of good seeing. The effective exposure time was 54.1 s. The five broad bands span the range from 3000 to 11,000 Å (Fukugita et al. 1996). The images were processed using specialized software (Lupton et al. 2001; Stoughton et al. 2002), and were photometrically (Tucker et al. 2006) and astrometrically (Pier et al. 2003) calibrated using observations of a set of primary standard stars (Smith et al. 2002) on a neighboring 20 inch telescope. The photometric calibration is accurate to roughly 2% rms in the *g*, *r*, and *i* bands, and 3% in *u* and *z*, as determined by the constancy of stellar population colors (Ivezić et al. 2004; Blanton et al. 2005). With the so-called "ubercalibration" (Padmanabhan et al. 2008), which uses overlap between imaging scans, the calibration residual errors are reduced to ∼2% in *u* and ∼1% in *griz*.

The majority of the SDSS imaging data are single-epoch images (except overlap regions between adjacent scans). But in addition to single-epoch data, the SDSS also conducted a deep survey by repeatedly imaging a ∼300 deg^2 area on the celestial equator in the south Galactic cap in the Fall (Adelman-McCarthy et al. 2007; Annis et al. 2011). This deep survey stripe, or Stripe 82, roughly spans $20^h < \text{R.A.} < 4^h$ and

[12] Visiting Astronomer, Kitt Peak National Observatory, National Optical Astronomy Observatory, which is operated by the Association of Universities for Research in Astronomy (AURA) under cooperative agreement with the National Science Foundation.
[13] Hubble Fellow.
[14] Stromlo Fellow.

$-1.^\circ26 <$ Decl. $< 1.^\circ26$. Stripe 82 was scanned 70–90 times, depending on R.A. along the stripe, in 1998–2007. In 1998–2004, roughly 80 SDSS imaging runs were taken on Stripe 82, usually under optimal observing conditions mentioned above. In 2005–2007, more than 200 additional runs were taken as part of the SDSS-II supernovae survey project (Frieman et al. 2008). The observing conditions for many runs in 2005–2007 were less optimal, with significant moonlight, poor seeing, or non-photometric transparency, as we will discuss in Section 2.1. The multi-epoch images of Stripe 82 are suitable for studies of variability and transient events. For example, they have been used for high-redshift supernovae survey (Frieman et al. 2008; Sako et al. 2008) and quasar variability studies (e.g., MacLeod et al. 2012; Schmidt et al. 2012). The multi-epoch data also allow the construction of deeper co-added images (Abazajian et al. 2009; Annis et al. 2011; Huff et al. 2011).

The first version of co-added images made from the Stripe 82 images are publicly available in the SDSS database. They were released in the SDSS Data Release 7 (Abazajian et al. 2009). The details of the construction of the co-adds are described in Annis et al. (2011). Briefly, Annis et al. (2011) combined images taken before 2005 December 1, over $-50^\circ <$ R.A. $< 60^\circ$ of the Stripe 82. Each area of sky included data from 20–35 runs. The co-added images were then run through the SDSS pipeline to generate catalogs and other standard SDSS products. The total coverage of the co-added catalog is 275 deg^2. The data are about 1–2 mag (depending on R.A. and bands) deeper than SDSS single-epoch data. Huff et al. (2011) also produced co-added images from the Stripe 82 data. Their products were mainly used for studies of galaxy weak lensing, so they only included images with relatively good seeing. In Jiang et al. (2009), we made our own co-added images that we used to select high-redshift ($z > 5$) quasars (Jiang et al. 2008, 2009; McGreer et al. 2013).

In this paper, we release a new version of the co-added images and their associated object catalogs. This version includes all available images that cover Stripe 82. The co-add methodology is slightly different from that of Annis et al. (2011). The main difference is that Annis et al. (2011) released catalogs of detected objects with properties measured by the standard SDSS pipeline, but we did not run the SDSS pipeline. Instead, we produced object catalogs using `SExtractor` (Bertin & Arnouts 1996). However, our images include many more SDSS runs than Annis et al. (2011), so they go considerably deeper. The additional runs we included were taken in 2006–2007 as part of the SDSS-II supernovae survey, as mentioned earlier. We also release near-IR J-band images that cover about 90 deg^2 of Stripe 82. These images were obtained from the NOAO Kitt Peak 4 m Mayall telescope, using the wide-field near-IR imager NEWFIRM (Probst et al. 2004). They have a depth of roughly 20.0–20.5 Vega mag (5σ detection for point sources), depending on position. This is much shallower than the depth of the co-added SDSS images, but represents a significant extension of the wavelength range covered by the SDSS filters.

In Section 2, we present the details of the construction of our co-added images from SDSS multi-epoch data. We then describe our image products and quality assessment in Section 3. In Section 4, we present our NEWFIRM J-band data. We summarize the paper in Section 5. Throughout the paper all SDSS magnitudes are on the AB system (not SDSS asinh magnitudes (Lupton et al. 1999); all asinh magnitudes have been converted to logarithmic AB magnitudes). The J-band magnitudes are on the Vega system.

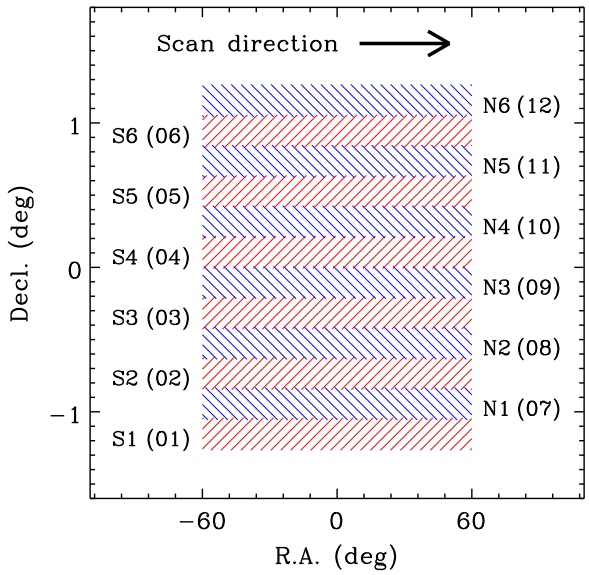

Figure 1. Layout of SDSS Stripe 82. Stripe 82 covers $-60^\circ <$ R.A. $< 60^\circ$ ($20^h <$ R.A. $< 4^h$) and $-1.^\circ26 <$ Decl. $< 1.^\circ26$. It consists of six south (S) scanlines (red hatch) and six north (N) scanlines (blue backward hatch). The numbers in the brackets are the scanline numbers used for our co-added images. (A color version of this figure is available in the online journal.)

2. CONSTRUCTION OF THE CO-ADDED IMAGES

In this section, we present the construction of our co-added Stripe 82 images. While there is no formal definition of the R.A. range for Stripe 82, we adopt the range of $-60^\circ <$ R.A. $< 60^\circ$ ($20^h <$ R.A. $< 4^h$) here. This range spans Galactic latitudes from $b = -15^\circ$ to $b = -63^\circ$. The fields near R.A. $= -60^\circ$ (or R.A. $= 300^\circ$) are close to the Galactic plane, so they are overwhelmed by Galactic stars and dust, and are not suitable for extragalactic studies. In addition, these fields have less scan coverage (and thus shallower co-added images), as we will see in the next section.

We started with all 314 runs that cover (part of) Stripe 82. An SDSS run (strip) consists of six parallel scanlines, identified by camera columns or "camcols," for each of the five *ugriz* bands. The scanlines are $13.'5$ wide, with gaps of roughly the same width, so two interleaving strips make a stripe. Figure 1 illustrates the two strips (12 scanlines) of Stripe 82, referred to as the south (S) and north (N) strips, respectively. In our final co-added data, the six S scanlines have scanline numbers from 01 to 06, and the six N scanlines have scanline numbers from 07 to 12 (Figure 1). SDSS scanlines are divided into fields. An SDSS field is the union of five *ugriz* frames covering the same region of sky, and a SDSS frame is a single image in a single band. The size of a field (or a frame) is 1489 × 2048 pixels, or roughly $9.'8 \times 13.'5$ (R.A. × Decl.), with a pixel size of $0.''396$. There is an overlap region with a width of 128 pixels along the scan direction between any two neighbor frames. The input images for our co-adds are SDSS calibrated frames, or the `fpC` images. These frames have been bias subtracted and flat-fielded, with bad and saturated pixels interpolated over.

2.1. Run and Field Selection

As the first step, we chose runs and fields for the Stripe 82 co-adds that are not of low quality (due to very poor seeing, high sky background, low sky transparency, etc.). For each field in the 314 runs between R.A. $= -60^\circ$ and 60°, we estimated three parameters from its r-band `fpC` frame: the FWHM of the

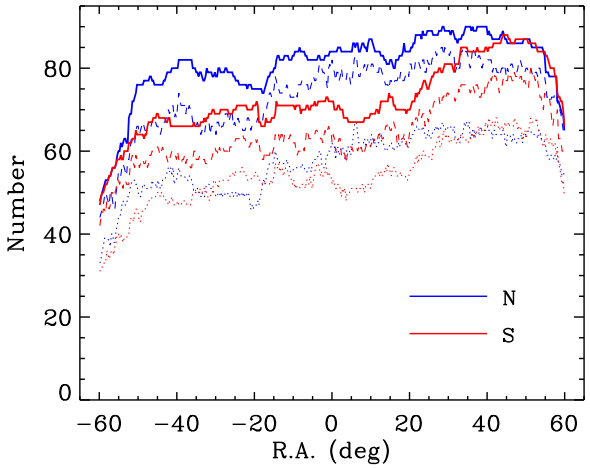

Figure 2. Run coverage (number of observing runs/scans) as a function of R.A. for Stripe 82. The north and south strips are indicated by blue and red, respectively. The solid lines represent the number of runs chosen for our co-adds. The median coverage is 82 for the N strip, and 71 for the S strip. The dashed and dotted lines represent the numbers of runs that were actually used for the co-adds (scanline 2 in N and S) in the *i* and *g* bands, respectively. See Section 2 for details.

(A color version of this figure is available in the online journal.)

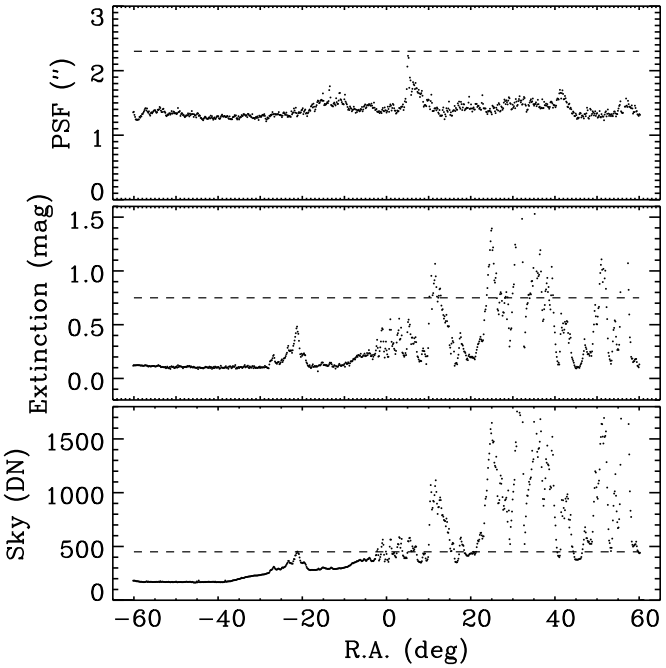

Figure 3. Some basic information for Run 7106 in the *r* band (scanline 6). From the top to the bottom panels we show PSF, atmospheric extinction, and sky background for each frame as a function of R.A. The dashed lines indicate our selection cuts. The image quality at R.A. $< -40^\circ$ in this run is good. The image quality is worse at R.A. $> -40^\circ$, and is unacceptable for the majority of the frames at R.A. $> 0^\circ$. Our procedure selected proper frames and weighted individual frames based on PSF, extinction, and background noise.

point-spread function (PSF), the atmospheric extinction (or sky transparency), and the sky background. The sky background is the median value of the frame, after the artificial soft bias of 1000 DN is subtracted. This value is consistent with the value provided by the keyword "sky" in the fits image header. More sophisticated sky subtraction is done later. In order to measure PSF FWHM and extinction, we ran `SExtractor` on the `fpC` frame, and measured PSF and flux (in units of DN) for isolated bright point sources. We then matched this object catalog to the catalog of Stripe 82 standard stars by Ivezić et al. (2007), and computed a zero point so that the median magnitude difference between the two catalogs is zero. This is the absolute zero point for this frame, regardless of whether the condition was photometric or non-photometric. So the magnitude of an object in this frame is $-2.5\log(\mathrm{DN}/t_{\rm exp})$ + zero point, where $t_{\rm exp}$ is the exposure time of 54 s. This procedure is the same as Annis et al. (2011) did, except that they used their own standard catalog. We found that the median zero point for data taken at photometric nights was 23.9 mag in the *r* band, the same as the value given by Annis et al. (2011). Finally, the relative atmospheric extinction is simply the zero-point offset from the photometric zero point. For the region that the Ivezić et al. (2007) catalog does not cover (R.A. $= 300^\circ - 306\overset{\circ}{.}5$), we chose one "good" Stripe 82 run with good seeing, low sky background, and nearly zero extinction as a standard run. We only took into account the relative extinction for the next steps.

Based on these three parameters, we rejected 11 runs in which most of the fields are of very low quality. The remaining 303 runs were used for our co-adds. They are listed in Table 3 in the Appendix. Figure 2 shows the number of runs as a function of R.A. (solid blue and red lines). The median coverages are 82 and 71 for the N and S strips, respectively. We kept runs even if only a small fraction of the fields are good. Figure 3 is an example, showing the three parameters in the *r* band for Run 7106. The frames at R.A. $< -40^\circ$ in this run have high quality, with a PSF of $\sim 1\overset{''}{.}3$, low extinction of $\sim$0.1 mag, and low sky background of $\sim$200 DN. The image quality then gets worse at R.A. $> -40^\circ$, and eventually becomes unacceptable at R.A. $> 0^\circ$. Our further selection criteria will select and weight individual frames based on the three parameters.

The SDSS CCDs were read out with two amplifiers. In some runs, the two amplifiers had different gains so that the two halves of an frame have obviously different background levels. We identified these runs (and frames) by comparing the background levels between the two halves and scaling (multiplying) one side of the frame to match the other side. This has negligible impact on the determination of extinction and the quality of final co-adds. The difference between the two halves is usually several DNs, and the fraction of affected frames is tiny ($\leqslant$2%, depending on scanline and filter).

In the next step we rejected frames with very poor seeing, high sky background, or high extinction. We required that seeing should be better than $2\overset{''}{.}3$ and extinction should be smaller than 0.75 mag in the *r* band (Figure 4). Although the cuts on seeing and extinction were made on the *r*-band frames, we rejected all associated data in the other four bands. However, unlike Annis et al. (2011), our selection cut on sky background was made on each band separately, rather than on just the *r* band. This is because the distributions of sky background for the five bands are very different, due to the fact that the dependence of sky background on is much more complex than the dependence of seeing or extinction on wavelength, especially under non-photometric observing conditions with significant moonlight or clouds. Figure 4 shows the distributions of sky background in the five bands. The difference between the distributions is obvious. For example, the *u*- and *g*-band distributions have very long tails at the high background end, but the *z*-band distribution does not show a long tail. Therefore, we set different cuts on sky background for different bands. We rejected frames with background higher than [80, 250, 450, 550, 250] in units of DN in the five bands. This is the result of a tradeoff between the

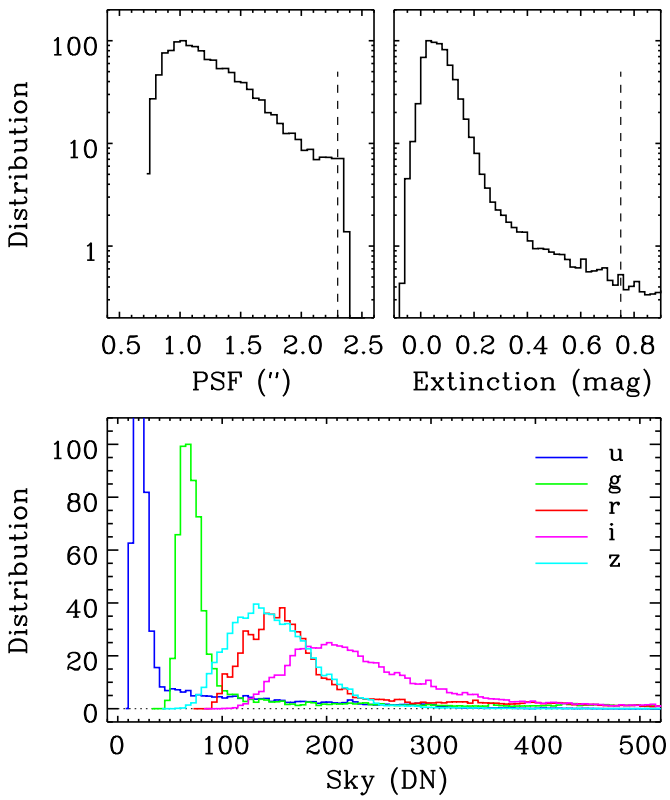

Figure 4. Distributions of PSF, extinction, and sky background. The two upper panels show the distributions of PSF and extinction measured in the *r* band. They have been normalized so that the peak values are 100. The vertical dashed lines indicate our selection cuts. The lower panel shows the distributions of sky background in the five bands. They have been normalized so that the peak value in the *g* band is 100. The distributions are very different in different bands, so our selection cuts on sky background were made on the individual bands, i.e., we rejected frames with background higher than [80, 250, 450, 550, 250] in the five bands, respectively.

(A color version of this figure is available in the online journal.)

background brightness and the number of frames to be rejected. The above cuts roughly correspond to [3.5, 3.5, 3, 2.5, 2.0] times the median background values in the five bands. The fractions of the frames rejected by the criteria are about [18%, 21%, 9%, 4%, 1%], respectively. This means that our final co-adds include more *z*-band frames than *u*.

Our selection criteria above are considerably more permissive than those of Annis et al. (2011), in order to include as many frames as possible and enhance the depth. The marginal gain (in terms of the depth of the co-adds) by changing the values in the criteria (to include more input frames) is negligible.

2.2. Sky Subtraction

The SDSS `fpC` frames do not have the sky background removed. We used a simple but efficient method to perform sky subtraction. Sky subtraction for the frames taken on moonless photometric nights are relatively easy, because the spatial and temporal variation across one SDSS field is small. It becomes more straightforward if a field does not have any large bright objects. In this case a low-order two dimensional function will provide a good fit to the background after objects are detected and masked out. However, a significant number of the runs were taken with moonlight and non-photometric conditions. They sometimes show strong background variation along the drift scan (R.A.) direction. Our background subtraction method was able to efficiently handle these extreme cases, as we now describe.

For each `fpC` frame, we ran `SExtractor` to detect objects after the soft bias was subtracted, and made a mask image accordingly. We set the detection threshold for objects to be 2σ in a minimum of 4 pixels. We divided the frame into 12×16 grid elements, where each element measures 128 pixels at a side. We calculated a sky value for each grid element from 256×256 pixels centered on this element, after the masked pixels were removed. This sky value was computed based on the distribution of the pixel values. We first calculated the mean and standard deviation of the sky pixels, which were then used to reject outliers. We repeated this process up to 20 iterations. If the mean was smaller than the median, then the mean was adopted for the sky value; otherwise the sky value was computed by $3 \times$ median $- 2 \times$ mean, an estimate for the mode of the distribution. If more than half of the pixels in a grid element were masked out (usually due to the presence of very bright/large objects), this element was flagged as "bad," and its closest neighbors were also flagged as "bad." The "bad" grid elements were not used.

The grid elements that were not flagged as "bad" could still be affected by "bad" elements. We corrected for this using a simple method. Although the sky varies along the drift scan direction (rows, or the R.A. direction), it is usually stable in the perpendicular direction (columns, or the decl. direction). A linear fit is a good description of the sky for each column for all but the worst data (which has already been rejected). However, if a grid element is affected by a very bright/large object, its sky value will deviate from the linear relation. We found the best linear relation for each column of 16 sky values (less than 16 if we already rejected some "bad" elements) in three iterations. In the first iteration we fit a simple linear relation to the data points. In the second iteration we fit a linear relation with a weight at each point. The weight at point *i* is proportional to an exponential function $1/\exp(s_i - s_i')$, where s_i is the measured sky value and s_i' is the value from the best linear fit in the first iteration. The exponential function strongly favors low values, which is consistent with the fact that lower values are almost always closer to real sky background. The third iteration repeated the algorithm from the second iteration, where the s_i' value in the weight was from the second iteration.

Figure 5 shows an example of sky fitting. The left is an `fpC` frame in the *i* band, with three columns (256 pixels wide) highlighted. The right plot shows the sky values (crosses) and their best linear fits (dotted and solid lines). In column A there is a large object, whose 3σ detection area extends more than $2'$ in diameter. Three grid elements of the sky have been flagged as "bad," and most elements in this column are affected by the presence of this object, as we can see from the big bump in the sky distribution. The dotted line is the best linear fit in the first iteration. The solid line is the best fit from the third iteration, and provides an excellent estimate of the real background. In column B, there are two bumps in the sky distribution, obviously due to the presence of the two bright objects. Although most of the grid elements in this column are affected by the two objects, our fitting process provides an excellent estimate of the sky. Column C in the figure exhibits an ideal case in which there are no bright stars in the whole column, so its 16 sky values can be well described by a simple linear fit in the first iteration.

After each grid element was replaced by the best linear fit in the column direction, the sky image was created by interpolating all pixels over the frame from the 12×16 sky values, using a minimum curvature spline surface. In order to save computing time, the spacing of the interpolation is 2×2 pixels, i.e., the resolution in the final sky image is 2×2 pixels ($0\farcs8 \times 0\farcs8$).

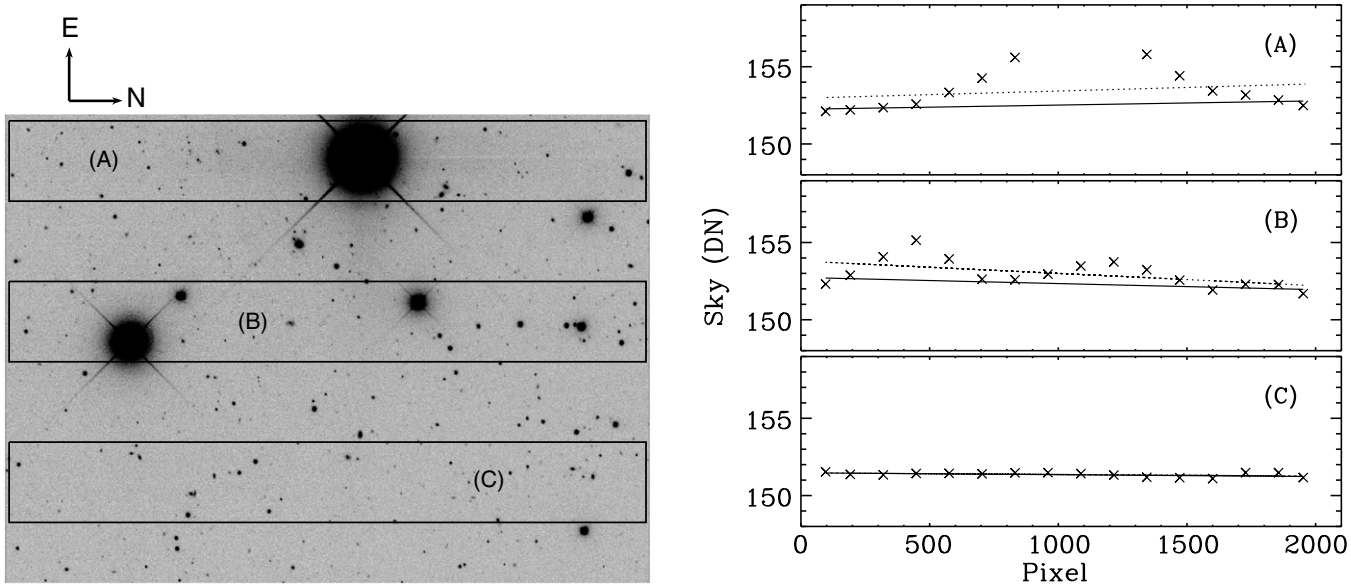

Figure 5. Example of sky fitting. The left is an `fpC` frame in the *i* band, and the right panel demonstrates the sky fitting for the three columns highlighted in the left image. The crosses represent sky values measured in grids of 256 × 256 pixels, after the masked pixels are removed. The dotted lines are the best linear fits from the first iteration of sky fitting. The solid lines are the best fits from the third or last iteration, and provide excellent estimates of real background. Note that for column C where there are no bright objects, the dotted and solid lines overlap.

The sky subtraction algorithms used by the SDSS pipeline `PHOTO` (Lupton et al. 2001) are similar to the first part of our method. `PHOTO` first detects and masks out bright objects, and computes sky values in grids of 256 × 256 pixels. These sky values are linearly interpolated to make a sky image, without further treatment of outliers. This could systematically underestimate the brightness of large objects. As shown in Figure 5, the bright object in column A is very extended. If we simply use the measured sky values (crosses), the sky around the object will be significantly overestimated, so that the brightness of the object is underestimated. Our fitting procedure can properly estimate the sky in the vicinity of this bright object. Our tests show that we can compute reasonable sky values unless objects are so large that they affect all sky grid elements in a column. Even in this case, our algorithm can still minimize the effect from bright objects.

Annis et al. (2011) used a different method to estimate sky background. They computed a median value for each column of pixels, and then fitted a linear relation to these median values along the row direction with sigma clipping in five iterations. This approach assumes that the sky is constant along the decl. direction and varies linearly along the R.A. direction. This is usually overly simplistic for images taken with significant moonlight or clouds. Our method is more sophisticated, by assuming a linear relation along the decl. direction and by allowing arbitrary sky variation along the R.A. direction.

2.3. Image Weights

Before we co-added the `fpC` frames, each input frame was assigned a weight proportional to

$$\frac{T^k}{\mathrm{FWHM}^m\ \sigma^n}, \tag{1}$$

where T is the sky transparency as measured by the extinction of the frame, FWHM is the FWHM of the PSF, σ is the standard deviation of the background noise (one constant value for a frame), and k, m, n are indices to be set for a specific science goal. In order to maximize the signal-to-noise ratios (S/Ns) of the sources in the co-added images, we set $k = 1$ and $n = 2$. In the *griz* bands, the noise in frames is completely dominated by sky background, so σ^2 is the variance of the sky background. In some *u*-band frames with very low sky background, however, read noise is not negligible. So we added read noise in quadrature to σ^2 in the *u* band.

For FWHM, it is difficult to determine an optimal m value for our co-adds. For point sources in individual frames in which sky background dominates the noise, the optimal m value is 2 (thus the depth is proportional to $1/\mathrm{FWHM}^2$), because the area occupied by an unresolved object scales with FWHM^2. However, for a co-added image with a large number of input frames and a wide range of PSF FWHM, the optimal m is less obvious. We carried out simulations based on artificial images and tests based on real Stripe 82 images, which showed that the S/N of the sources in co-adds is very insensitive to m in the range $0.5 < m < 2$. Considering that the PSF FWHM is less important for more extended sources, we chose $m = 1$ for FWHM instead of $m = 2$. In summary, the indices we chose are $k = 1$, $m = 1$, and $n = 2$, thus the weight is proportional to $T/(\mathrm{FWHM}\,\sigma^2)$. This is different from the weight $(T/(\mathrm{FWHM}^2\,\sigma^2))$ used by Annis et al. (2011).

For each input frame, we read the list of defective pixels, i.e., those affected by cosmic rays and bad columns, from the associated `fpM` file, and assigned them a near-zero weight (1.0^{-10}). We also assigned this near-zero weight to the overlap region (128 pixel wide) between one frame and its following neighbor frame. After that, a weight image was created for each input frame.

2.4. Co-addition

We divided each scanline along $-60^\circ < \mathrm{R.A.} < 60^\circ$ into 401 regions each with a size of 2850 × 2048 pixels. The pixel size is the same as the native size of 0.″396. There is also a common area of 128 pixels between each region and its following neighbor region. The size of the regions is twice the size of the SDSS `fpC` frames when the overlap area is removed. This reduces the total

number of output co-added images by a factor of two, but still allows one to easily split one co-added image into two images with the fpC frame size. As we described in Section 2.1, we rejected frames based on PSF, extinction, and sky background. At this stage, we made a final selection cut for each region in each band, removing any frames with weights below 0.4 times the median weight of the frames belonging to that region. This removed $\leqslant$2% of frames.

With the corrected input fpC frames and their weight maps, the construction of co-adds is straightforward. We scaled the frames by $1/T$, and re-sampled them to a common astrometric grid using SWARP (Bertin et al. 2002). Note that reliable astrometric solutions (better than 45 mas rms; Pier et al. 2003) have been incorporated into SDSS fpC frames. The re-sampling interpolations for the science and weight images were lanczos3 and bilinear, respectively. We then co-added images using SWARP. The co-addition is a weighted mean with outlier rejection (7σ). The output products include a co-added science image and its associated weight image for each region. The weight images record relative weight at each pixel position.

The main differences between our co-adds and those of Annis et al. (2011) are as follows. First, our co-adds include many more SDSS runs, but our selection of runs and fields is more permissive. Second, the sky subtraction algorithms and image weights are slight different. Finally, Annis et al. (2011) produced catalogs of objects with the SDSS pipeline, but we produced object catalogs with SExtractor (Section 3.2).

3. DATA PRODUCTS

Because of our selection cuts on PSF, extinction, and sky background, the actual number of SDSS frames used in the co-adds varies from region to region. In Figure 2, the blue (red) dashed and dotted lines show the number of frames used for the co-adds of N (S) scanline 2 in the i and g bands, respectively. The number of frames used for i is 60–70, and for g is 50–60. These numbers are more than twice larger than those used in Annis et al. (2011). For each filter, the fraction of frames used in our co-adds is roughly constant with right ascension. For example, this fraction is ~90% in the i band and ~75% in the g band. In this section, we will introduce our final data products and provide some basic statistical information for the co-adds.

3.1. Photometric Calibration

Although atmospheric extinction was measured and corrected for individual input frames, it was not very accurate for frames with large extinction and/or high sky background due to the small numbers of high S/N point sources (especially in the u and z bands). So we determined photometric calibration on the co-added images. As we did in Section 2.1, we ran SExtractor on each co-added image and performed aperture photometry for point sources within an aperture (diameter) size of 20 pixels (8″). Blended objects were rejected. We then matched this object catalog to the Ivezić et al. (2007) catalog, and computed a zero point (the median magnitude difference of the matched objects between the two catalogs is zero). For simplicity, we already assumed the exposure time of 1 s for the zero points, so the magnitude of an object is simply −2.5 log(DN) + zero point. For the region of sky that the Ivezić et al. (2007) catalog does not cover, we applied an average zero point for each scanline. The zero points were recorded in the image headers as "magzero."

In Figure 6 we show the distributions of the magnitude differences between the aperture magnitudes of the co-added images and the PSF magnitudes from the Ivezić et al. (2007) catalog for a subset of our data (R.A. = 330°–30°; scanline 08). The σ values are from the best Gaussian fits, and have a range from 0.012 to 0.020. These magnitude differences are likely caused by the combination of the different algorithms use to measure aperture and PSF magnitudes and the photometric errors or calibration. For comparison, in the right bottom panel we show the distribution of the difference between the aperture (7.″4 radius) and PSF magnitudes for bright ($i < 19$) stars from SDSS single-epoch data. Its σ value is 0.031.

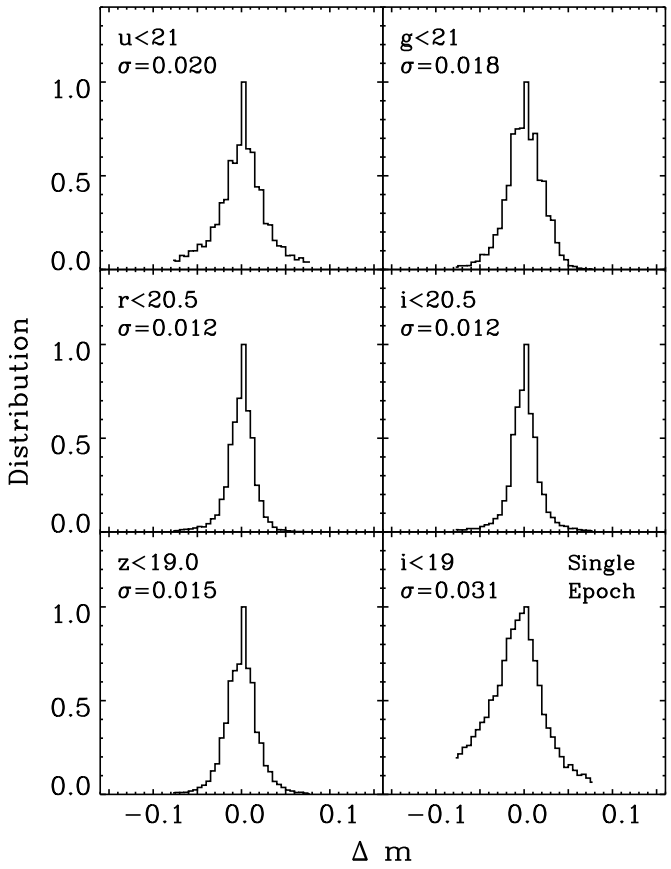

Figure 6. Distributions of the differences between the aperture (4″ radius) magnitudes of the co-added images and the PSF magnitudes from the Ivezić et al. (2007) catalog (R.A. = 300°–30°; scanline 08). The distributions have been normalized so that the peak values are 1. The σ values are from the best Gaussian fits. The right bottom panel shows the difference between the aperture (7.″4 radius) and PSF magnitudes for bright ($i < 19$) stars from SDSS single-epoch data.

3.2. Images and Catalogs

Our final products consist of 24,060 science images (12 scanlines × 5 filters × 401 regions) and their associated weight images and catalogs. The science and weight images are called "S82_xxy_zzz.fits" and "S82_xxy_zzz.wht.fits," where "xx" is the scanline number from 01 to 12 (Figure 1), "y" is the filter, and "zzz" is the region number from 001 to 401. For example, "S82_08i_234.fits" and "S82_08i_234.wht.fits" are the co-adds for scanline 08 (N scanline 2), filter i, and region 234.

We also produced object catalogs from these data. The catalogs are named "S82_xxy_zzz.cat," and were produced by SExtractor. The key part of the SExtractor configuration file is displayed in Table 1. Briefly, we detected objects in a minimum of four contiguous pixels (DETECT_MINAREA) with a detection threshold of 2σ (DETECT_THRESH). SExtractor

Table 1
SExtractor Configuration File

Keyword	Value
CATALOG_TYPE	ASCII_HEAD
DETECT_MINAREA	4
DETECT_THRESH	2
DEBLEND_NTHRESH	16
DEBLEND_MINCONT	0.002
WEIGHT_TYPE	MAP_WEIGHT
PHOT_APERTURES	6, 8, 10, 12, 20
PHOT_AUTOPARAMS	2.5, 3.5
PHOT_PETROPARAMS	2.0, 3.5

took the weight images produced by SWARP as input weight images (WEIGHT_TYPE) during its procedure of object detection. SExtractor deblending is done using a multi-thresholding algorithm. It deblends components of a composite detection at up to DEBLEND_NTHRESH levels based on local detection peaks, where DEBLEND_NTHRESH is the number of deblending sub-thresholds. At each level, DEBLEND_MINCONT is the minimum contrast parameter for deblending, i.e., any new component with flux larger than DEBLEND_MINCONT (times the total flux of the current "parent" component) is considered as a new component for the next level of deblending. We performed aperture photometry within five diameter aperture (PHOT_APERTURES) sizes of [6, 8, 10, 12, 20] pixels (2.″4, 3.″2, 4.″0, 4.″8, and 8.″0). We also computed "AUTO" magnitudes (Kron-like elliptical aperture magnitudes; the best for extended sources from SExtractor) and Petrosian magnitudes with the default parameters (PHOT_AUTOPARAMS and PHOT_PETROPARAMS).

The complete list of the quantities computed for the catalogs is shown in Table 2. Each catalog can be roughly divided into three parts. The first part shows the positions and coordinates of detected objects. The second part lists various magnitudes and errors. The third part provides some basic information about object structure and morphology, including semimajor and semiminor axes, ellipticity, FWHM, etc. The last parameter "FLAGS" is the SExtractor extraction flag, the sum of powers of 2. For example, "1" (2^0) means that an object is very close to bright objects or bad pixels so that its photometry could be significantly affected. "2" (2^1) means that an object is blended with other objects. The detailed explanations for the keywords and parameters in Tables 1 and 2 can be found in Bertin & Arnouts (1996) and the SExtractor user's manual. There are several caveats on how to use these catalogs.

1. There is overlap between one region and its following neighbor region, so any object detected in this overlap area will show up in two catalogs. In addition, any two adjacent scanlines also slightly overlap, and these are independent detections.
2. The catalogs are not matched between the bands, resulting in different object lists for each band within the same region. The deblending of an object in different bands could also be different.
3. The object detection threshold is 2σ in a minimum of 4 pixels, so objects fainter than this are not included. One example is very low surface brightness galaxies. In order to detect such galaxies, one may convolve the images with a kernel.
4. Users need to apply aperture corrections before aperture magnitudes can be used across different bands (e.g., for constructing color–color diagrams). Aperture corrections are different for different regions in different bands (depending on wavelength and PSF). A good approximation for point sources within a given aperture is the median difference between the aperture magnitudes within this aperture and the aperture magnitudes within 20 pixels for bright isolated point sources from the catalogs (aperture corrections from 20 pixels to infinite are smaller than 0.5%).
5. Measurements of objects that are several pixels away from image edges are not reliable. Because these objects are in the overlap area between adjacent regions or scanlines, better measurements can be found in the adjacent catalog where the object is less near to the edge.
6. Transient objects and objects with high proper motions have been eliminated by the use of outlier rejection when co-adding the images. Also note that many single-band detections are spurious detections, usually associated with diffraction and bleed spikes from bright stars. These spikes can be faint in the co-adds (invisible in input SDSS frames), but extend across more than one image.

Table 2
SExtractor Parameter File

Parameters	Units	Description
NUMBER	···	Running object number
X_IMAGE	pixel	Object position along x
Y_IMAGE	pixel	Object position along y
ALPHA_J2000	deg	R.A. (J2000)
DELTA_J2000	deg	Decl. (J2000)
MAG_APER	mag	Aperture mag
MAGERR_APER	mag	Error for MAG_APER
MAG_AUTO	mag	Auto mag (Kron-like elliptical aperture mag)
MAGERR_AUTO	mag	Error for MAG_AUTO
MAG_PETRO	mag	Petrosian mag (Petrosian-like elliptical aperture mag)
MAGERR_PETRO	mag	Error for MAG_PETRO
A_IMAGE	pixel	Semi-major axis
B_IMAGE	pixel	Semi-minor axis
THETA_IMAGE	deg	Position angle
ELLIPTICITY	pixel	Ellipticity: 1-B_IMAGE/A_IMAGE
KRON_RADIUS	···	Kron radius in units of A_IMAGE
PETRO_RADIUS	···	Petrosian radius in units of A_IMAGE
FWHM_IMAGE	pixel	FWHM assuming a Gaussian core
FLAGS	···	Internal extraction flags; sum of powers of 2

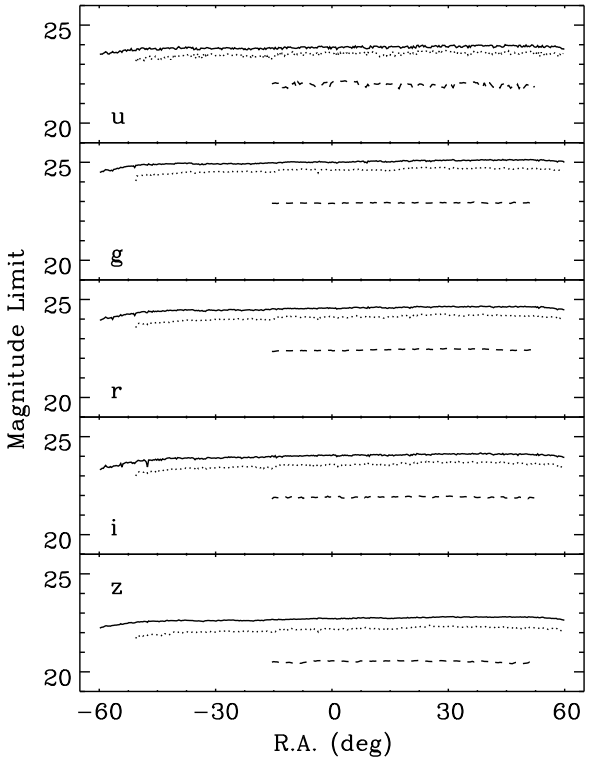

Figure 7. 5σ detection limits of the aperture (3.″2 diameter) magnitudes for point sources in scanline 08 of the co-adds (solid lines). The dotted lines are the magnitude limits for the Annis et al. (2011) co-adds, and the dashed lines are the magnitude limits for single-epoch (Run 4263) data. Run 4263 is one of the best runs for Stripe 82. Our co-adds are 1.9–2.2 mag deeper than the best SDSS single-epoch data, and 0.3–0.5 mag deeper than the Annis et al. (2011) co-adds.

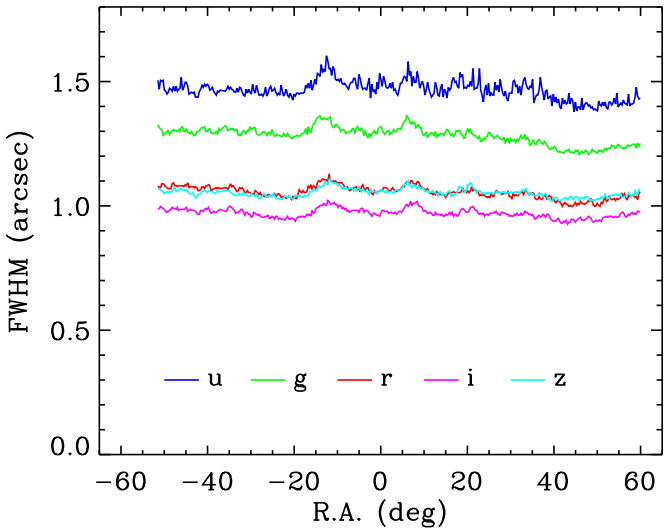

Figure 9. PSF FWHM in the five bands in scanline 08 (N scanline 2) of the co-adds. The PSF FWHM in the *riz* bands is roughly 1″, and in the *ug* bands is about 1.″3–1.″5.

(A color version of this figure is available in the online journal.)

7. Our catalogs only included commonly used quantities, usually with default setup parameters. If users need more quantities, or quantities with different parameters, they are advised to run `SExtractor` (or other tools) on the co-added images by themselves.

3.3. Depth

We determine the depth of our co-added data based on the aperture magnitudes within an aperture (diameter) size of 8 pixels (3.″2). As the photometric uncertainties depend on aperture size, our choice of 8 pixels, or two to three times the PSF FWHM, represents a tradeoff between reducing the aperture correction and reducing background noise. In Figure 7 we show the magnitude limits of the 5σ detection (i.e., photometric errors = 0.22) for point sources in scanline 08 (solid lines). Our co-added images have great depth of roughly 23.9, 25.1, 24.6, 24.1, and 22.8 AB magnitudes in the five bands, respectively. The magnitude limits are compared to the magnitude limits of the Annis et al. (2011) co-adds (dotted lines) and of the single-epoch (Run 4263) data (dashed lines). Run 4263 is one of the best runs for Stripe 82, taken on a photometric dark night with excellent seeing (PSF $\sim$ 0.″8 in the *r* band). The magnitude limits for all three different data sets were computed using the same method, i.e., aperture photometry within an aperture of 8 pixels. Compared to Run 4263, our co-adds are 1.9, 2.1, 2.1, 2.1, and 2.2 mag deeper in the *ugriz* bands, respectively. Our co-adds are also 0.3–0.5 mag deeper than the co-adds of Annis et al. (2011). Figure 8 shows a direct comparison between a single-epoch frame in the *i* band (left), the Annis et al. (2011) co-add (middle), and our co-add (right).

Figure 9 shows the PSF FWHM in the five bands in scanline 08 of the co-adds. The PSF FWHM was measured with `SExtractor` based on bright point sources. Note that PSF measurements from different methods (such as SDSS, `SExtractor`, or `IRAF`) can be slightly different due to the different algorithms used. The *i*-band images in the co-adds have the PSF with the smallest FWHM, and the *u*-band images have the worst PSF. The *r*- and *z*- band images have similar PSF sizes. In addition,

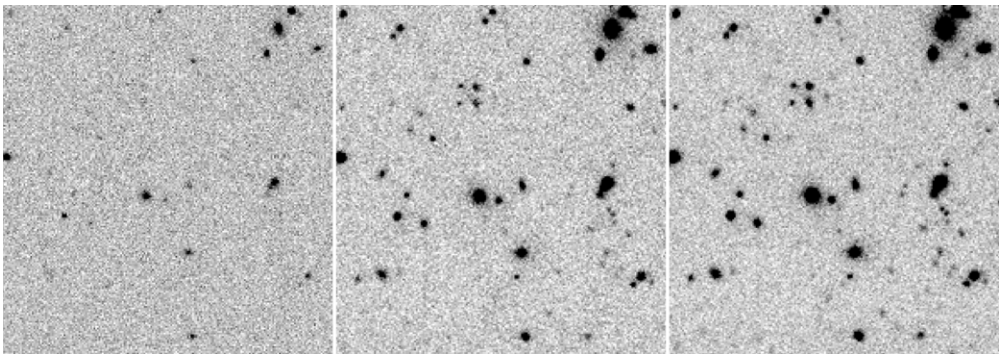

Figure 8. Direct comparison between a single-epoch *i*-band frame (left panel), the Annis et al. (2011) co-add (middle panel), and our co-add (right panel). The PSF sizes are similar (0.″8–0.″9). The image size is 1.′3 × 1.′3 located at $21^{h}29^{m}30^{s}$–$00^{d}32^{m}20^{s}$.

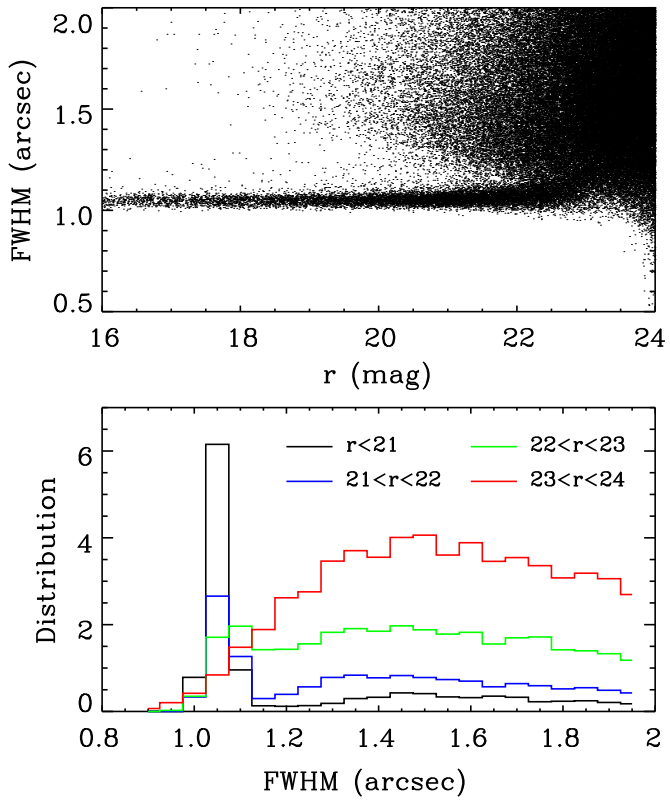

Figure 10. Star–galaxy separation. The upper panel shows the object size (FWHM) as a function of the brightness in r (R.A. = 10^h–30^h; scanline 08). The narrow strip clearly indicates the location of stars. The lower panel shows the FWHM distribution. At $r < 22$ mag, stars are well separated. They start to mix with galaxies at $r > 22$ mag, and are completely mixed with galaxies at $r > 23$ mag. In this example, we use FWHM $< 1''.12$ to separate stars from galaxies.

(A color version of this figure is available in the online journal.)

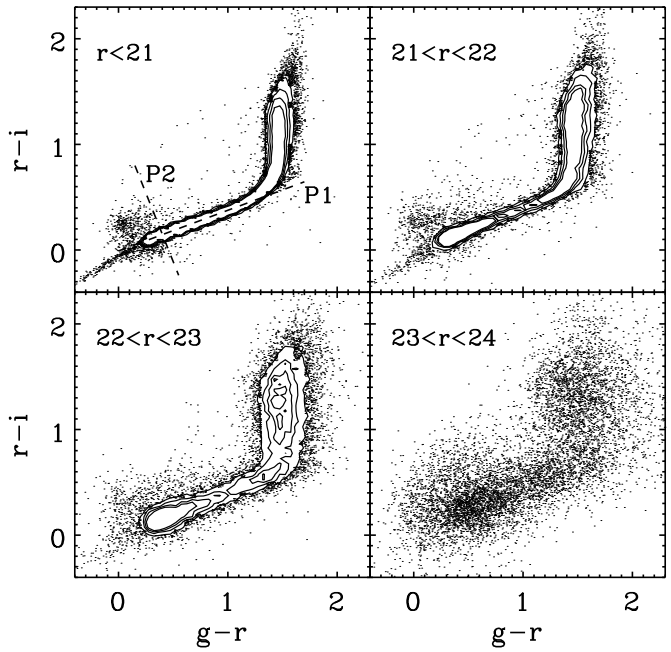

Figure 11. $r - i$ vs. $g - r$ color–color diagram for point objects brighter than $r = 24$ mag selected in Figure 10. In the first panel we also define two principal axes, P1 and P2. P1 is along the blue part of the stellar locus and P2 is perpendicular to P1. They are used to quantify the width of the stellar locus (see Section 3.4 and Figure 12).

the PSF varies across scanlines due to the camera optics. SDSS scanline 6 (scanlines 06 and 12 in our co-adds) has the worst PSF in most bands. Figure 9 shows that the PSF FWHM in the *riz* bands is roughly $1''$, and in the *ug* bands is between $1''.3$ and $1''.5$. These numbers are consistent with those of single-epoch data with the best observing conditions, and are also consistent with the co-adds of Annis et al. (2011).

3.4. Color–Color Diagrams

SDSS point sources are mostly main sequence stars, which form a tight stellar locus in color–color diagrams (Ivezić et al. 2004). The width of the stellar locus is almost independent of magnitude, but is broadened by photometric errors of stars, so color–color diagrams are a useful tool for photometric quality assessment. We first separate stars (point sources) from galaxies (extended sources). The SDSS uses the difference between PSF magnitude and so called "model" magnitude to do star–galaxy separation. As we did not run the SDSS pipeline, we did not measure these magnitudes. Instead, we separate stars and galaxies based on the distribution of object sizes (FWHM) as measured by `SExtractor`. Figure 10 shows an example. The upper panel shows the object size (FWHM) as the function of the brightness in r (R.A. = 10°–30°; scanline 08). The object detection and photometry are described in Section 3.3. The narrow horizontal band in the plot clearly demonstrates the location of stars. The width of this band is dominated by the small variation of the PSF across the scanline. The lower panel shows the distribution of the object sizes. At $r < 22$ mag, stars in this example can be well separated using FWHM $< 1''.12$. They start to mix with galaxies at $r > 22$ mag, and are completely mixed with galaxies at $r > 23$ mag, as seen in the both panels. However, we still use FWHM $< 1''.12$ to separate stars from galaxies at $r > 23$ mag.

In Figure 11 we show the $r - i$ versus $g - r$ color–color diagram for point objects brighter than $r = 24$ mag selected in Figure 10. The objects are grouped into four magnitude bins. As expected, the stellar locus in the brightest bin ($r < 21$ mag) is very tight. It becomes broader in fainter bins, as photometric errors start to dominate the width. In the third bin ($22 < r < 23$), the stellar locus still has a well-defined shape, though it is much broader. In the faintest bin, the stellar locus is not as obvious as it appears in the brighter bins, due to large photometric errors and leakage of a large number of galaxies, since the star–galaxy separation does not work well at the faintest end (Figure 10).

We quantify the width of the stellar locus in Figure 11 following the method of Helmi et al. (2003) and Ivezić et al. (2004). We focus on the width of the blue part in the $r - i$ versus $g - r$ diagram, and define two principal axes, P1 and P2. As shown in the first panel of Figure 11, P1 is along the locus and P2 is perpendicular to P1. P2 is further adjusted for a weak dependence on r. The w color is then defined on P1 and P2 as the distance from a star to P1. The distribution of w describes the width of the stellar locus. The results are shown in Figure 12, where the stars brighter than $r = 23$ mag from Figure 11 are grouped into four bins. The σ values are from the best Gaussian fits, and have a range from 0.016 (brightest bin) to 0.061 (faintest bin). Ivezić et al. (2004) reported that the rms of w at $r < 20$ mag is 0.025 mag for SDSS single-epoch data, and decreases to 0.022 mag for data with observations at several epochs. We reached $\sigma = 0.019$ mag at $r < 22$ mag, indicating that our co-adds are indeed at least two mag deeper than single-epoch data. Ivezić et al. (2007) also reported a rms of w of

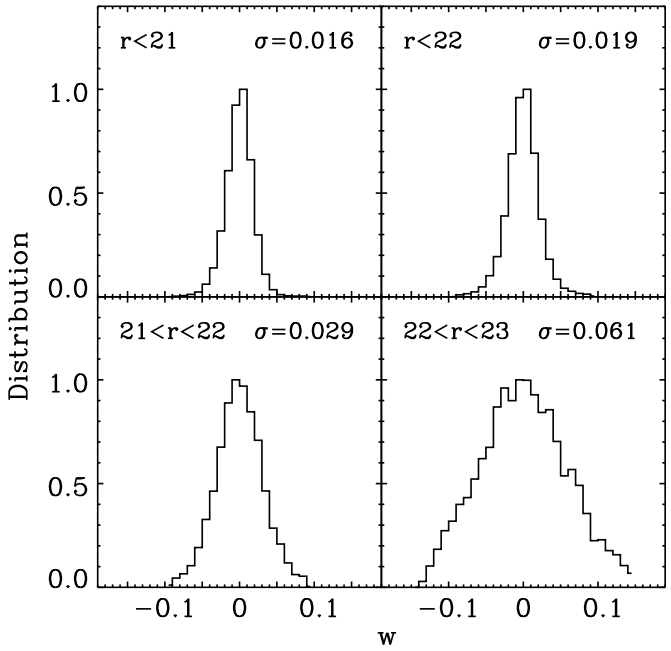

Figure 12. Distributions of the w colors for the stars brighter than $r = 23$ mag in Figure 11. The distributions have been normalized so that the peak values are 1. The σ values are from the best Gaussian fits. The value of σ (0.019 mag) at $r < 22$ is smaller than the rms of w at $r < 20$ for SDSS single-epoch data, indicating that the co-adds are at least two mag deeper than single-epoch data.

$\sigma = 0.010$ mag at $r < 20$ mag for data with multi-epoch ($\geqslant$10) observations. We achieved 0.016 mag at $r < 21$ mag and could not obtain a smaller σ for brighter stars, suggesting the existence of a calibration floor in the data. This was likely caused by the difference between the aperture magnitudes of the co-adds and the PSF magnitudes of the Ivezić et al. (2004) catalog during the process of photometric calibration (Section 3.1 and Figure 6).

4. NOAO/NEWFIRM *J*-BAND IMAGING DATA

In addition to the SDSS data in five optical bands, Stripe 82 is also (partially) covered by surveys/observations at many other wavelengths, such as the UKIRT Infrared Deep Sky Survey (UKIDSS; Lawrence et al. 2007), the Very Large Array imaging of Stripe 82 at 1.4 GHz (Hodge et al. 2011), and the *Herschel* Stripe 82 Survey (Viero et al. 2014). In this section we present our near-IR *J*-band observations with NOAO NEWFIRM (Probst et al. 2004). NEWFIRM is a wide-field infrared imager with a field of view of $27' \times 27'$ (pixel size $0''.4$), mounted at the f/8 R-C focus of the NOAO 4 m telescopes. Our NEWFIRM observations were made with the Kitt Peak 4m Mayall telescope. They cover $\sim$90 deg^2 of Stripe 82 to a depth of 20–20.5 Vega mag.

4.1. Observations and Data Reduction

The NEWFIRM observations were made in two runs on 2007 November 10–16 and 2009 January 6–15. The observing conditions in the two runs were moderate, with mostly clear skies and a large range of seeing from $\sim 1''$ to $> 2''.5$. In the 2007 run, we observed $\sim$150 fields (NEWFIRM pointings). A typical observing strategy was a 3×3 dither pattern (dither offset $40''$). The exposure time at each dither position was 30 s or 60 s, depending on sky background. This pattern was conducted twice with slightly different central positions for data taken with an exposure time of 30 s. The total integration time was thus 540 s per field. In the 2009 run, we observed $\sim$300 fields. We used a dither pattern with five positions (dither offset $45''$). At each dither position we took six short (15 s) exposures. The short exposures were co-added internally and read out as one image. The total integration time per field was also 540 s. Note that this ability to do internal co-addition had not been embedded in the NEWFIRM observing pipeline during the 2007 run. Adjacent fields slightly overlapped by $1'$–$2'$. Several fields were observed twice due to low image quality. We also rejected a small fraction of images that were taken with very poor observing conditions.

The NEWFIRM data were reduced with the combination of our `IDL` routines and the IRAF[15] NEWFIRM task by M. Dickinson and F. Valdes. The basic procedure is summarized as follows. We first reduced calibration data, and made master dark and dome flat images for each night. Each science image was then trimmed and a dark frame was subtracted, followed by linearity correction and flat fielding. A weight image was created by assigning a near-zero number (10^{-10}) to defective pixels, such as bad pixels, saturated pixels, and persistence. The weight image did not include seeing or sky transparency. Unlike the Stripe 82 images that were taken under very different observing conditions, the NEWFIRM images for any single field were taken under similar conditions within a span of $\sim$10 minutes. Sky subtraction was done using a similar method to the one we used for the SDSS images. After sky background was subtracted, we detected objects using `SExtractor`, and calculated astrometric solutions using `SCAMP` (Bertin 2006) by matching objects to the SDSS. Finally we used `SWARP` to re-sample and stack images, as we did for the SDSS images. The re-sampling interpolations for science and weight images were lanczos3 and bilinear, respectively. The co-addition is a weighted mean with outlier rejection (5σ). The products are one co-added science image and its associated weight image for each field. The weight image records relative weight at each pixel position.

4.2. Photometric Calibration and Data Products

We performed photometric calibration using the method that we did for the SDSS co-adds. Briefly, we ran aperture photometry within an aperture (diameter) size of 20 pixels ($8''$). Blended objects were rejected. We then matched to the Two Micron All Sky Survey (2MASS; Skrutskie et al. 2006) point source catalog, and computed a zero point for each image. For simplicity, we already assumed the exposure time of 1 s for the zero point, so the magnitude of an object is simply -2.5 log(DN) + zero point. The zero point was recorded in the image headers as "magzero."

Figure 13 compares the calibrated NEWFIRM data and the 2MASS point source catalog (red histogram). The NEWFIRM data displayed in this figure were taken on one 2007 night and one 2009 night. The 2MASS objects were chosen to be brighter than $J = 15.5$ mag. The rms of the magnitude difference is $\sigma = 0.054$, meaning that our photometric calibration is accurate to about 5%. We also compared the NEWFIRM data with the UKIDSS data (blue histogram). The UKIDSS objects were chosen to be point sources between $J = 17$ and 18 mag. The distribution of the magnitude difference is consistent with the red histogram. Note that UKIDSS is roughly three magnitudes deeper than 2MASS, and was also calibrated using the 2MASS catalog.

[15] IRAF is distributed by the National Optical Astronomy Observatory, which is operated by the Association of Universities for Research in Astronomy (AURA) under cooperative agreement with the National Science Foundation.

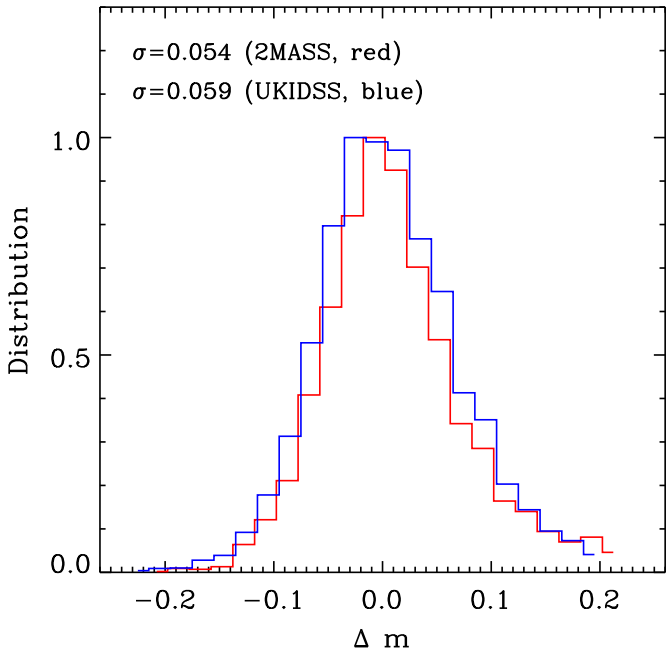

Figure 13. Quality of the photometric calibration for the NEWFIRM data. The histograms show the comparison of the calibrated NEWFIRM data with 2MASS (red) and UKIDSS (blue). The 2MASS objects are point sources brighter than $J = 15.5$ mag, and the UKIDSS objects are point sources between $J = 17$ and 18 mag. The σ values (rms of the distributions) are from the best Gaussian fits. The figure indicates that our photometric calibration is accurate to about 5%–6%.

(A color version of this figure is available in the online journal.)

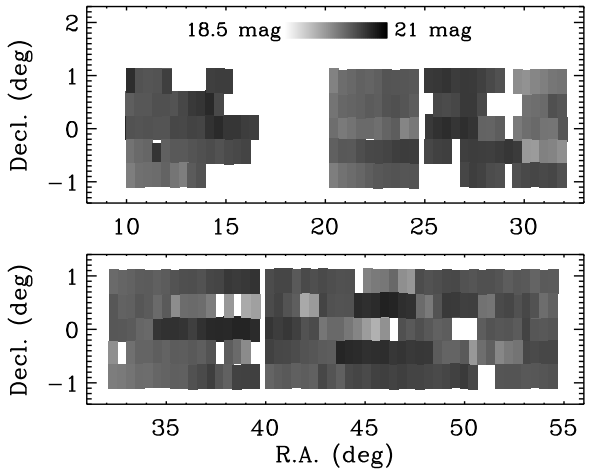

Figure 14. Layout of the NEWFIRM pointings and the depth of the *J*-band images. The depth is the 5σ detection limit for point sources.

The final data products include 450 stacked images and the associated weight images and catalogs. The image size is 4300 by 4300 pixels, and the pixel size is the same as the native size of 0.″4. The area at image edges (∼100 pixels) have much lower coverage due to the dithering of the observations. When this is taken into account, the effective area of each image is about 0.2 deg^2. So our final products cover roughly 90 deg^2 of Stripe 82, in the range of $10^\circ <$ R.A. $< 55^\circ$. Figure 14 shows the layout of the NEWFIRM pointings along with the image depth (the next subsection). The catalogs were produced in the same way as we did for the SDSS images (Section 3.2). The `SExtractor` configuration and parameter files are also the same as shown in Tables 1 and 2, except the aperture sizes.

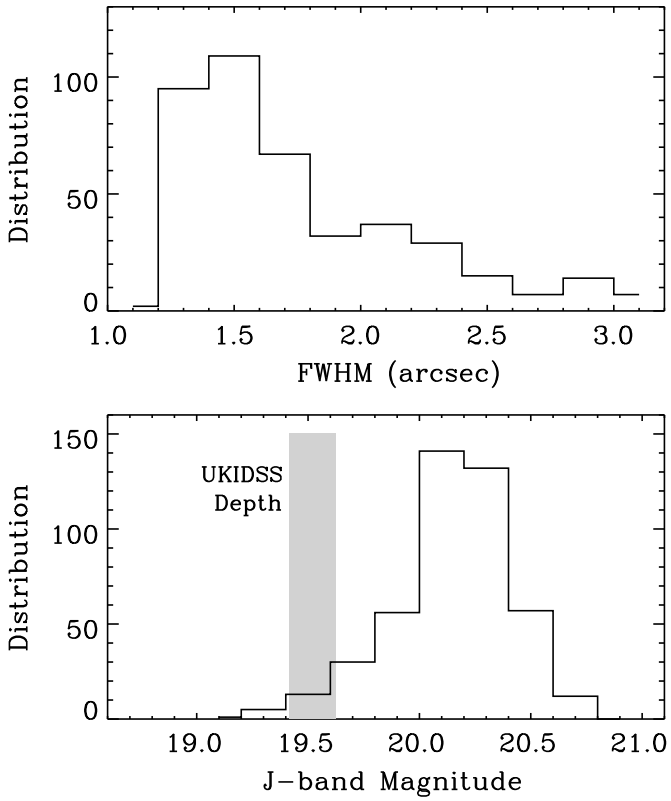

Figure 15. Upper panel: distribution of PSF FWHM in our NEWFIRM *J*-band images. Lower panel: distribution of the image depth for point sources. The grey shaded region shows the UKIDSS *J*-band depth in Stripe 82 (see details in Section 4.3). Our NEWFIRM images are about 0.7 mag deeper on average.

We used the five sizes of [8, 10, 12, 14, 20] pixels for aperture magnitudes.

4.3. Depth and Color–Color Diagrams

We measure the depth of the images in the same way as we did for the SDSS data. The depth is described as the 5σ detection limit for point sources. The photometry was measured in one of four apertures (diameter) [8, 10, 12, 14] pixels (3.″2–5.″6), because of the range of image quality in these data. The upper panel in Figure 15 shows the distribution of the PSF FWHMs. Many PSF FWHMs are larger than 2″ due to poor seeing and unstable instrument focus in 2007. The lower panel in Figure 15 shows the distribution of the image depth. While the distribution spans a wide range from 19 to 21 mag, most images have a depth of 20–20.5 mag. For comparison, the grey shaded region shows the UKIDSS depth (single epoch) in the *J* band in Stripe 82. The depth is also the 5σ detection limit, derived from ∼100,000 point sources centered at R.A. = 10°, 20°, 30°, and 40° (decl. = 0°). The left and right boundaries of the shaded region indicate the 1σ range of the detection limit distribution. On average, our *J*-band images are ∼0.7 mag deeper than the UKIDSS images.

Compared to the SDSS co-added images, however, the *J*-band images are significantly shallower (Figure 16). The depth of the SDSS co-adds shown in Figure 7 is 24–25 mag in $ugri$, and is ∼22.8 mag in z. The *J*-band depth is 20–20.5 Vega mag, or 21–21.5 AB mag. This is 1.5 ∼ 3 mag shallower.

Figure 17 shows the $z - J$ versus $i - z$ color–color diagram for point sources brighter than $J = 20$ mag in the region between R.A. = 40° and 55°. The point sources are selected using the distribution of object FWHMs in the *J* band. Like the stellar

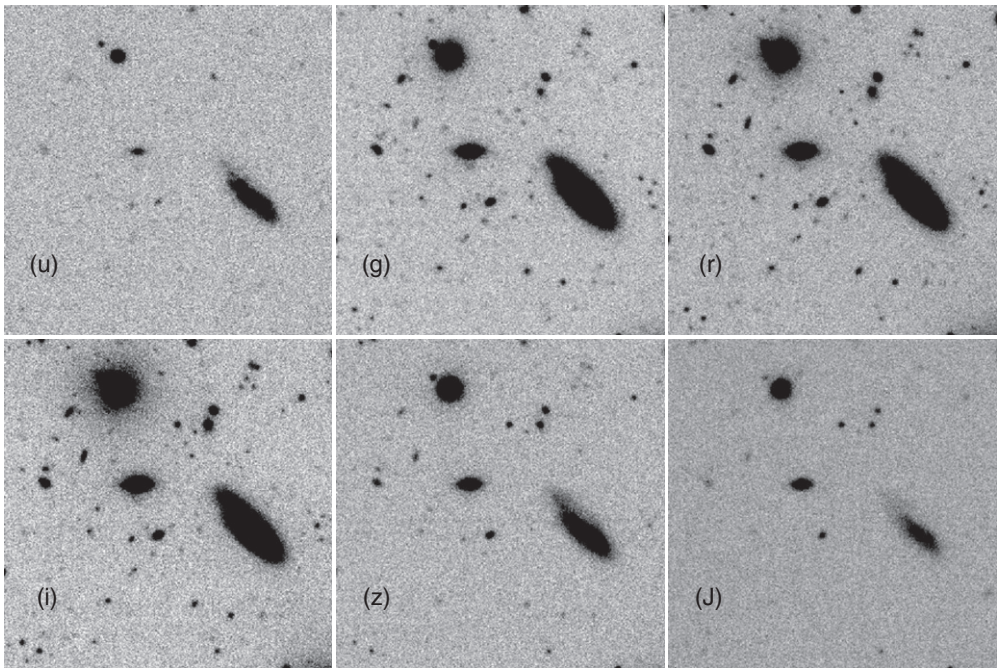

Figure 16. Direct comparison between the SDSS optical data and the NEWFIRM *J*-band data. The image size is $2' \times 2'$ located at $00^h50^m01^s$+$00^d35^m24^s$. The *J*-band image was chosen to have a depth of 20.2 mag (the average depth of our *J*-band images) with a relatively good PSF of $1''.5$ (see Figure 15). The SDSS co-adds are deeper than the NEWFIRM images.

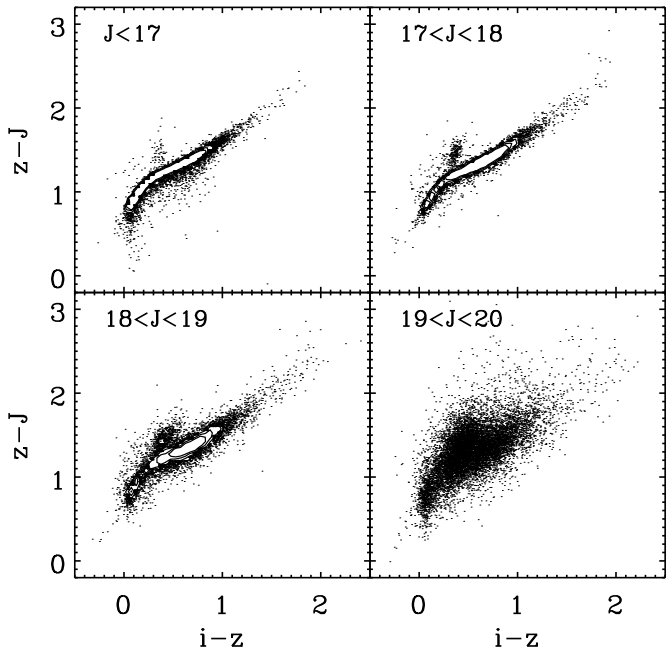

Figure 17. $z-J$ vs. $i-z$ color–color diagram for point objects brighter than $J = 20$ mag in the region between R.A. $= 40°$ and $55°$. There is a distinct clump of data points at $i-z = 0.35$ and $z-J = 1.45$ that are away from the stellar locus. These sources are compact galaxies that were identified as stars due to the poor image quality in the *J*-band data.

locus in the $r-i$ versus $g-r$ diagram, the stellar locus in the $z-J$ versus $i-z$ diagram is very tight in the brightest magnitude bin of $J < 17$ mag. It becomes broader in fainter bins, as photometric errors increase. Since the *i*- and *z*-band data are much deeper than the *J*-band data, the photometric errors in the diagram are dominated by the *J*-band errors. In the faintest bin ($J > 19$ mag), the stellar locus is not obvious any more due to large photometric errors and leakage of a large number of galaxies, as we saw in the faintest bin in the $r-i$ versus $g-r$ diagram. There is also a distinct clump of data points at $i-z = 0.35$ and $z-J = 1.45$ that are away from the stellar locus. It is not seen in the color–color diagrams of stars in previous studies (e.g., Finlator et al. 2000). These sources are compact galaxies. The majority of them are classified as extended sources by the SDSS. However, they were selected as stars by the *J*-band data due to the poor seeing.

5. SUMMARY AND DATA RELEASE

In this paper we have introduced a new version of co-added images for the SDSS Stripe 82. Stripe 82 covers 300 deg^2, and was repeatedly scanned 70–90 times over roughly 10 years. These Stripe 82 images, when co-added, reach a much greater depth than do SDSS single-run data. We have described the details of the construction of our co-added images. In order to optimize the depth of the co-adds, we considered all available data in the SDSS archive and included as many images as possible, so that the marginal gain by adding more images is negligible. Each input image was properly processed and weighted based on PSF FWHM, sky transparency, and background noise. In particular, we performed sky subtraction using a simple but efficient method that can properly deal with the presence of large objects and strong background variation along the drift scan direction. Our final products consist of 24,060 science images and their associated weight images and object catalogs. The weight images record relative weight at each pixel position. The catalogs were made with `SExtractor`. Our co-adds reach more than two mag deeper than the deepest SDSS single-epoch images, and 0.3–0.5 mag deeper than the Annis et al. (2011) co-adds. They have good image quality with an average PSF FWHM of $\sim 1''$ in the *r*, *i*, and *z* bands. We have also presented *J*-band images obtained from NOAO NEWFIRM. These images cover roughly 90 deg^2 of Stripe 82 and have a depth of 20.0–20.5 Vega magnitudes.

Our co-added images have many potential uses for studies of galaxies, quasars, and Galactic structure. The advantage of the data is the uniform coverage over 300 deg^2 of the sky to a great depth. Annis et al. (2011) has listed many science opportunities, from Galactic dwarf stars to galaxy clusters. Here we briefly present two science cases not considered by Annis et al. (2011). The first science case is high-redshift quasars, including quasars at $z \sim 6$ and $z \sim 5$. So far we have found 13 $z \sim 6$ quasars down to $z \simeq 22$ mag (10σ detection) in Stripe 82 (Jiang et al. 2008, 2009). Six of them are fainter than the depth of the Annis et al. (2011) co-adds. The critical part of the selection of these quasars is the $z - J$ versus $i - z$ color–color diagram, so J-band data such as our NEWFIRM data are also important to find $z \sim 6$ quasars. Our co-adds have also been used to find $z \sim 5$ quasars (McGreer et al. 2013). These quasars are two magnitudes fainter than those found in the SDSS single-epoch data, and allow us to probe the faint end of the quasar luminosity function at this redshift. The second science case is to find high-redshift Lyman-break galaxies (LBGs) at $z \geqslant 3$ using the dropout technique. These distant galaxies are usually very faint and only found in deep small-area (several square degrees or smaller) surveys. Our co-adds are deep enough to find bright LBGs at $z \geqslant 3$, given that the 5σ depth in the r band (24.6 mag) reaches the characteristic luminosity L^* of $z = 3$ LBGs. In particular, their sky coverage is large enough to find ultra-luminous LBGs (more than two magnitudes brighter than L^*) like the one reported by Bian et al. (2012). Furthermore, the co-adds are likely more efficient to select bright LBGs at $z \sim 4$ based on the $g - r$ color, because the g band is the deepest SDSS band.

All our data products, including co-added science images and their associated weight images and object catalogs, are released on this Web site: http://das.sdss.org/ge/sample/stripe82/. The "Readme" file on the Web site describes the structure of the data set and how to download the data. The SDSS co-added data are under the folder or link "sdss," and the NEWFIRM data are under the folder or link "newfirm." In addition, we will work on high-level catalogs with functions such as searchable tables and the cross-match of multiple bands. We will release these products on the same Web site when they are ready.

Support for this work was provided by NASA through Hubble Fellowship grant HST-HF-51291.01 awarded by STScI, which is operated by the Association of Universities for Research in Astronomy, Inc., for NASA, under contract NAS 5-26555. L.J. also acknowledge support from the National Natural Science Foundation of China (NSFC) under grants 11003021 and 11373003. X.F. and I.D.M. acknowledge support from Packard Fellowship for Science and Engineering and NSF grant AST 08-06861 and AST 11-07682. Z.B. acknowledges financial support from Princeton University to travel to Kitt Peak.

Funding for the SDSS and SDSS-II has been provided by the Alfred P. Sloan Foundation, the Participating Institutions, the National Science Foundation, the U.S. Department of Energy, the National Aeronautics and Space Administration, the Japanese Monbukagakusho, the Max Planck Society, and the Higher Education Funding Council for England. The SDSS Web site is http://www.sdss.org/.

The SDSS is managed by the Astrophysical Research Consortium for the Participating Institutions. The participating institutions are the American Museum of Natural History, Astrophysical Institute Potsdam, University of Basel, University of Cambridge, Case Western Reserve University, University of Chicago, Drexel University, Fermilab, the Institute for Advanced Study, the Japan Participation Group, Johns Hopkins University, the Joint Institute for Nuclear Astrophysics, the Kavli Institute for Particle Astrophysics and Cosmology, the Korean Scientist Group, the Chinese Academy of Sciences (LAMOST), Los Alamos National Laboratory, the Max-Planck-Institute for Astronomy (MPIA), the Max-Planck-Institute for Astrophysics (MPA), New Mexico State University, Ohio State University, University of Pittsburgh, University of Portsmouth, Princeton University, the United States Naval Observatory, and the University of Washington.

Facilities: Sloan, Mayall (NEWFIRM)

Table 3
SDSS Runs Used for Our Co-adds

Run	MJD	$\text{Field}_{\text{start}}$	$\text{Field}_{\text{end}}$	$\text{R.A.}_{\text{start}}$	R.A._{end}	Strip
125	51081	11	586	−9.45	76.57	S
1033	51464	11	244	−41.30	−6.42	N
1056	51467	12	232	−34.00	−1.05	S
1752	51818	40	372	26.84	76.55	N
1755	51819	74	683	−45.23	45.95	S

(This table is available in its entirety in a machine-readable form in the online journal. A portion is shown here for guidance regarding its form and content.)

APPENDIX

SDSS RUNS USED FOR OUR CO-ADDS

Table 3 shows the SDSS runs selected for our co-adds of Stripe 82. The first two columns are SDSS run numbers and MJD. Columns 3 and 4 show the starting and ending fields. Columns 5 and 6 show the starting and ending R.A. in degrees. The last column indicates that a run consists of south (S) or north (N) strips for Stripe 82.

REFERENCES

Abazajian, K. N., Adelman-McCarthy, J. K., Agüeros, M. A., et al. 2009, ApJS, 182, 543
Adelman-McCarthy, J. K., Agüeros, M. A., Allam, S. S., et al. 2007, ApJS, 172, 634
Ahn, C. P., Alexandroff, R., Allende Prieto, C., et al. 2012, ApJS, 203, 21
Ahn, C. P., Alexandroff, R., Allende Prieto, C., et al. 2014, ApJS, 211, 17
Annis, J., Soares-Santos, M., Strauss, M. A., et al. 2011, arXiv:1111.6619
Bertin, E. 2006, in ASP Conf. Ser. 351, Astronomical Data Analysis Software and Systems XV, ed. C. Gabriel, C. Arviset, D. Ponz, & E. Solano (San Francisco, CA: ASP), 112
Bertin, E., & Arnouts, S. 1996, A&AS, 117, 393
Bertin, E., Mellier, Y., Radovich, M., et al. 2002, in ASP Conf. Ser. 281, Astronomical Data Analysis Software and Systems XI, ed. D. A. Bohlender, D. Durand, & T. H. Handley (San Francisco, CA: ASP), 228
Bian, F., Fan, X., Jiang, L., et al. 2012, ApJ, 757, 139
Blanton, M. R., Schlegel, D. J., Strauss, M. A., et al. 2005, AJ, 129, 2562
Eisenstein, D. J., Weinberg, D. H., Agol, E., et al. 2011, AJ, 142, 72
Finlator, K., Ivezić, Ž., Fan, X., et al. 2000, AJ, 120, 2615
Frieman, J. A., Bassett, B., Becker, A., et al. 2008, AJ, 135, 338
Fukugita, M., Ichikawa, T., Gunn, J. E., et al. 1996, AJ, 111, 1748
Gunn, J. E., Carr, M., Rockosi, C., et al. 1998, AJ, 116, 3040
Gunn, J. E., Siegmund, W. A., Mannery, E. J., et al. 2006, AJ, 131, 2332
Helmi, A., Ivezić, Ž., Prada, F., et al. 2003, ApJ, 586, 195
Hodge, J. A., Becker, R. H., White, R. L., Richards, G. T., & Zeimann, G. R. 2011, AJ, 142, 3
Hogg, D. W., Finkbeiner, D. P., Schlegel, D. J., & Gunn, J. E. 2001, AJ, 122, 2129
Huff, E. M., Hirata, C. M., Mandelbaum, R., et al. 2011, arXiv:1111.6958
Ivezić, Ž., Lupton, R. H., Schlegel, D., et al. 2004, AN, 325, 583
Ivezić, Ž., Smith, J. A., Miknaitis, G., et al. 2007, AJ, 134, 973
Jiang, L., Fan, X., Annis, J., et al. 2008, AJ, 135, 1057
Jiang, L., Fan, X., Bian, F., et al. 2009, AJ, 138, 305
Lawrence, A., Warren, S. J., Almaini, O., et al. 2007, MNRAS, 379, 1599

Lupton, R., Gunn, J. E., Ivezić, Z., Knapp, G. R., & Kent, S. 2001, in ASP Conf. Proc. 238, Astronomical Data Analysis Software and Systems X, ed. F. R. Harnden, Jr., F. A. Primini, & H. E. Payne (San Francisco, CA: ASP), 269
Lupton, R. H., Gunn, J. E., & Szalay, A. S. 1999, AJ, 118, 1406
MacLeod, C. L., Ivezić, Ž., Sesar, B., et al. 2012, ApJ, 753, 106
McGreer, I. D., Jiang, L., Fan, X., et al. 2013, ApJ, 768, 105
Padmanabhan, N., Schlegel, D. J., Finkbeiner, D. P., et al. 2008, ApJ, 674, 1217
Pâris, I., Petitjean, P., Aubourg, É., et al. 2012, A&A, 548, A66
Pâris, I., Petitjean, P., Aubourg, É., et al. 2014, A&A, 563, A54
Pier, J. R., Munn, J. A., Hindsley, R. B., et al. 2003, AJ, 125, 1559
Probst, R. G., Gaughan, N., Abraham, M., et al. 2004, Proc. SPIE, 5492, 1716
Sako, M., Bassett, B., Becker, A., et al. 2008, AJ, 135, 348
Schmidt, K. B., Rix, H.-W., Shields, J. C., et al. 2012, ApJ, 744, 147
Skrutskie, M. F., Cutri, R. M., Stiening, R., et al. 2006, AJ, 131, 1163
Smith, J. A., Tucker, D. L., Kent, S., et al. 2002, AJ, 123, 2121
Stoughton, C., Lupton, R. H., Bernardi, M., et al. 2002, AJ, 123, 485
Tucker, D. L., Kent, S., Richmond, M. W., et al. 2006, AN, 327, 821
Viero, M. P., Asboth, V., Roseboom, I. G., et al. 2014, ApJS, 210, 22
York, D. G., Adelman, J., Anderson, J. E., Jr., et al. 2000, AJ, 120, 1579